UKAEA-CCFE-PR(23)140

Luca Stefanescu, Max Boleininger, Pui-Wai Ma

Athermal swelling and creep of heavily irradiated iron under uniaxial stress

Athermal swelling and creep of heavily irradiated iron under uniaxial stress

Luca Stefanescu, Max Boleininger, Pui-Wai Ma

This is a preprint of a paper submitted for publication in
Physical Review Materials

Athermal swelling and creep of heavily irradiated iron under uniaxial stress

Luca Stefanescu[*]
University College London, Department of Physics,
Gower St, London, WC1E 6BT, United Kingdom

Max Boleininger and Pui-Wai Ma[†]
United Kingdom Atomic Energy Authority, Culham Science Centre,
Abingdon, Oxfordshire, OX14 3DB, United Kingdom

We investigated the athermal irradiation-induced swelling and creep in iron subjecting to the application of external uniaxial stress. We studied this through atomic scale simulations using the creation-relaxation algorithm. We also calculated the defect relaxation volume density tensors (or eigenstrain) as a function of external uniaxial stress. Beyond the dose value corresponding to isolated defects formation, interstitial-type defect clusters form with polarization causing crystal growth in the direction where tensile stress is applied, and growth in the other two perpendicular directions when a compressive stress is applied. The microstructure in terms of the concentrations of vacancies, isolated self-interstitial atoms, Laves phases clusters, and dislocations is not much affected by the external stress, up to at least ±1 GPa. The main cause of the biased crystal growth is due to the anisotropic formation of new crystal planes due to coalescence of interstitial defect clusters. Extra lattice planes form and lead to plastic deformation according to the direction and magnitude of the external stress.

I. INTRODUCTION

Iron and steels are important materials with a wide range of domestic and industrial applications. Reduced activation ferritic-martensitic (RAFM) steels are chosen as the structural materials of advanced fission and fusion reactors [1, 2]. RAFM steels have a body-centered cubic (bcc) crystal structure, which is the same as pure iron. A main reason for choosing RAFM steels is because they show less swelling under neutron irradiation compared to austenitic steels with face-centered cubic (fcc) structure [3]. Commercial ferritic steels are highly resistant to swelling even at extreme exposure to irradiation, showing less than 2% volume change under irradiation at 420°C up to 200 DPA [4].

Inside a fission or fusion reactor, nuclear reactions generate high energy neutrons which can penetrate deep inside a reactor component. These neutrons are scattered by atoms constituting the component, during which they transfer a fraction of their kinetic energy to the recoiling atoms. If sufficient energy is transferred, a recoil atom becomes a ballistic particle in itself, initiating a cascade of atomic collisions. The total exposure of a material to irradiation is measured in units of displacement per atom (DPA) [5], which is the number density of atoms ballistically displaced by collision cascades. In metals, accumulation of atomic displacements results in the formation of complex microstructures containing defects, such as self-interstitial atoms, vacancies, voids, dislocation loops and dislocation lines [6–12]. The change of microstructure can degrade both the thermal [13–15] and mechanical [16, 17] properties of materials, affecting the lifetime of components.

Neutron irradiation experiments of RAFM steels up to 70 DPA in a fission reactor at 330-340°C [18] show irradiation causing hardening and embrittlement, with saturation of these effects occurring at high doses. Dislocation loops with Burgers vector of $\frac{a}{2}\langle 111\rangle$ and $a\langle 100\rangle$ are commonly observed [4, 19], where their relative abundances depend on the irradiation conditions and alloy composition. RAFM steel will be used as the first wall material of the demonstration (DEMO) fusion plants, which are expected to experience lifetime neutron irradiation doses between 1 to 10 DPA [20]. Besides, Gilbert *et al.* [21] performed neutron transport calculations. Depending on the design and position of the first wall made of Eurofer, the rate of damage accumulation can range from 8 to 20 DPA per full power year.

In real operating conditions, components of fission and fusion plants can be subjected to applied tensile or compressive stresses due to gravity or magnetic field. Misalignment of components due to human operation or swelling of materials in limited space can also cause enormous stress to materials. Stress-induced anisotropic dimensional change is referred as creep [22]. Numerous phenomenological models [23, 24] based on assumed microstructure evolution were proposed to explain irradiation-induced creep and swelling.

As it is technologically challenging to monitor changes in materials properties in an extreme radiation environment *in-situ*, computer simulations have the potential to improve our understanding of materials behavior under irradiation. While state-of-the-art molecular dynamics (MD) simulations of consecutive collision cascades can feasibly reach doses of 1 DPA [25, 26], these type of simulations are computationally intensive. For system sizes that can accommodate the formation of extended dislo-

---

[*] lucastu2013@gmail.com
[†] Corresponding author: Leo.Ma@ukaea.uk

cation microstructure, requiring to the order of a million atoms [27], it is prohibitively expensive to conduct a comprehensive collision cascade study across a parameter space with multiple stochastically independent simulations.

Recent atomic scale simulations adopted the creation-relaxation algorithm (CRA) [28] which allows examination of irradiation damage in the order of 1 to 10 DPA. CRA is a parameter-free and assumption-free algorithm. In CRA, an atomic displacement is generated in the form of a Frenkel pair by choosing a random atom and moving it to an arbitrary position. Then, one can relax the atomic configuration through minimization of total energy. This accumulates $1/N$ DPA, where N is the number of atoms in a simulation cell. The microstructure evolves according to the spatial fluctuation of stresses induced by defects.

Using CRA, Derlet and Dudarev [28] studied the saturation of defects production in Fe and W. They also studied the spatial fluctuation of stresses and the spontaneous reorganization of microstructure. Tian *et al.* [29] and Warwick *et al.* [30] studied the anisotropic swelling of zirconium due to the formation of a- and c-type dislocation loops. Mason *et al.* [31] explained the negative lattice strain being detected by spatially resolved X-ray Laue diffraction in self-ion irradiated tungsten. Using a combination of CRA and MD, Mason *et al.* [32] accurately estimated the deuterium retention capacity in heavily irradiated tungsten. Chartier and Marinica [33] used the Frenkel Pair Accumulation (FPA) method to study high dose irradiation damage in bcc iron. FPA is similar to CRA, but it relaxes the atomic configuration through dynamic evolution. They observed nucleation of C15 clusters at the early stage, which can transform into $\frac{a}{2}\langle 111\rangle$ and $a\langle 100\rangle$ dislocation loops.

Recently, Reali *et al.* [34] suggested that one can compute the macroscopic stress and strain on the component scale using the defect relaxation volume density tensor $\boldsymbol{\omega}$, which can be obtained from atomic scale simulations, such as CRA or MD. They proved analytically that the relaxation volume density tensor is equivalent to the eigenstrain $\boldsymbol{\epsilon}^*$ of defects. Since the spatially varying eigenstrain can be interpreted as a source of an effective body force [34], one can solve the constitutive equation, and calculate the dimensional changes, through finite element method (FEM).

In this work, we adopted the CRA to study the effect of external uniaxial stress on defect production and crystal growth in pure iron that realized as irradiation-induced swelling and creep. Iron is the major component of steels and has the same crystal structure as RAFM steels. We will examine the effect quantitatively through calculating the defect relaxation volume density tensor $\boldsymbol{\omega}$ (or eigenstrain $\boldsymbol{\epsilon}^*$). We will also study the microstructural change in detail. The anisotropic changes of $\boldsymbol{\omega}$ will be explained through observation of the microstructure evolution and the deformation of simulation cells.

II. THEORY

A. Simulation setup

We performed our simulations using cells containing 1,024,000 atoms. Each cell contains $80 \times 80 \times 80$ bcc unit cells, with each unit cell containing 2 atoms. The potential energy of iron atoms is described by the interatomic potential developed by Ackland *et al.* [35].

We intended to simulate the condition of a material subjected to external uniaxial stress. However, a simulation cell with periodic boundary conditions has no free surface that one can apply external force on. Therefore, we simulated such condition by deforming the simulation cells, driving the Virial stress [36] to attain certain values. This is in principle equivalent to the application of external uniaxial stress, provided that the Virial stress equals to the Cauchy stress.

We initialized simulation cells under uniaxial stress by deforming them gradually through energy minimization using the conjugate gradient method. The cell vectors were kept orthogonal. Cells were deformed until the stress in the z direction equals 0, ± 0.00001, ± 0.00002, ± 0.00005, ± 0.0001, ± 0.0002, ± 0.0005, ± 0.001, ± 0.01, ± 0.02, ± 0.05, ± 0.1, ± 0.2, ± 0.5, or ± 1 GPa, and stresses in the x and y directions equal to zero. We use a sign convention such that positive stress means tensile stress in the z direction, and negative means compressive.

All simulations were performed using LAMMPS [37]. Irradiation damage was simulated according to the CRA. Throughout the entire simulation process, simulation cell vectors are allowed to deform under the constraints of keeping the initial uniaxial stress unchanged, and of keeping the cell vectors orthogonal. For each uniaxial stress value, we performed 3 identical simulations using different random numbers as seeds for the stochastic process of choosing random atoms and moving them to random locations. Data are presented as the average of 3 samples.

B. Creation-relaxation algorithm

We should note the meaning of DPA here is different from the conventional definition of NRT-DPA by Norgett, Robinson and Torrens [5]. In CRA, the meaning of DPA is taken literally as it incrementally introduces damage in the form of Frenkel pairs by *displacing* random atoms to random positions. This is corresponding to low temperature conditions where diffusion of defects is inhabited. Albeit the difference of definition, Derlet and Dudarev [28] and Warwick *et al.* [30] showed in Fe & W and Zr, respectively, that the saturation behaviors of swelling due to accumulation of defects can be obtained quantitatively through rescaling. Recent ion irradiation experiment [38] on tungsten also show good quantitative agreement with CRA prediction.

In the work by Derlet and Dudarev [28], CRA was implemented such that upon displacement of an atom, a dose of $1/N$ dpa is accumulated, where N is the number of atoms in the simulation cell. Frenkel pairs were created one by one, and after each creation of a Frenkel pair the atomic configuration was relaxed through energy minimization. Subsequent work using CRA [29–32] showed that creation of multiple Frenkel pairs per relaxation step, corresponding to a dose increment of 10^{-3} DPA per relaxation step or more, can speed up the simulation and have little effect on the results.

In our implementation, we created Frenkel pairs corresponding to a dose increment of 10^{-3} DPA per relaxation step. In each relaxation step, we first relaxed the atomic configuration without changing the shape of a simulation cell. Then, we relaxed the atomic configuration together with the simulation cell, until the Virial stress attained the target values. This is to guarantee the numerical stability in the energy minimization procedure. We repeat this procedure until all samples reach 3 DPA.

C. Defect relaxation volume density tensor

The concept of eigenstrain $\boldsymbol{\epsilon}^*$ was introduced by Mura [39]. Eigenstrain is a generic term referring to nonelastic internal strain. Reali *et al.* [34] proved analytically that the defect relaxation volume density tensor $\boldsymbol{\omega}$ is equivalent to the eigenstrain due to the existence of defects. In the absence of other sources of nonelastic strain, one can write:

$$\epsilon^*_{ij}(\mathbf{x}) = \omega_{ij}(\mathbf{x}). \tag{1}$$

The defect relaxation volume density tensor can be defined as [34]:

$$\omega_{ij}(\mathbf{x}) = \sum_a \Omega^a_{ij}\delta(\mathbf{x} - \mathbf{R}_a), \tag{2}$$

where Ω^a_{ij} is the relaxation volume tensor of a defect situated at $\mathbf{R}_a$. The relaxation volume tensor, together with the elastic constants, can describe the elastic properties of a defect in the asymptotic limit far from the defect. The values of Ω_{ij} of various defects can be obtained using density function theory calculations [40–44] and molecular statics [45, 46].

Knowing the spatially varying $\boldsymbol{\omega}(\mathbf{x})$, one can calculate the effective body force [34, 47]:

$$f_i(\mathbf{x}) = -C_{ijkl}\frac{\partial \omega_{kl}(\mathbf{x})}{\partial x_j}. \tag{3}$$

where C_{ijkl} is the elastic stiffness tensor. This body force can be supplied to a continuum model, such as the finite element method (FEM), for calculations in the component scale.

We should note that component-scale simulations using FEM describe spatial scales many orders of magnitude larger than atomistic simulations. Assuming a component having a dimension of 1 m^3, if one considers 1 million finite elements, the linear dimension of an element is 1 cm, which is much larger than atomic scale simulations using Å or nm as unit. Consequently, if we are interested in engineering simulations, we only need certain homogenized information for an element without knowing the details of microstructure. On the other hand, we remain interested in understanding the changes of macroscopic properties due to microstructural evolution from a scientific perspective.

Following Mura [39], the total strain is expressed as the sum of eigenstrain and elastic strain:

$$\epsilon_{ij}(\mathbf{x}) = \epsilon^*_{ij}(\mathbf{x}) + \epsilon^e_{ij}(\mathbf{x}). \tag{4}$$

Assuming linear elasticity, the stress is related to the elastic strain through Hooke's law:

$$\sigma_{ij}(\mathbf{x}) = C_{ijkl}\epsilon^e_{kl}(\mathbf{x}). \tag{5}$$

Since eigenstrain equals to the relaxation volume density tensor, one can write the stress:

$$\sigma_{ij}(\mathbf{x}) = C_{ijkl}\left(\epsilon_{kl}(\mathbf{x}) - \omega_{kl}(\mathbf{x})\right). \tag{6}$$

Taking the average over the whole simulation cell, the average stress is

$$\bar{\sigma}_{ij} = C_{ijkl}(\bar{\epsilon}_{kl} - \bar{\omega}_{kl}). \tag{7}$$

After rearranging terms, one can write

$$\bar{\omega}_{ij} = \bar{\epsilon}_{ij} - S_{ijkl}\bar{\sigma}_{kl}, \tag{8}$$

where S_{ijkl} is the elastic compliance tensor, which is the inverse of the elastic stiffness tensor C_{ijkl} [48]. In this work, C_{ijkl} is calculated from the interatomic potential. The average strain $\bar{\epsilon}_{ij}$ can be obtained according to the change of the simulation cell vectors. The average stress $\bar{\sigma}_{kl}$ is the applied stress.

Our applied stress only has one nonzero component in the z direction. Using the compliance tensor appropriate for bcc crystal symmetry, the average relaxation volume density tensor can be simplified to:

$$\bar{\boldsymbol{\omega}} = \begin{pmatrix} \bar{\epsilon}_{11} - S_{1133}\bar{\sigma}_{33} & 0 & 0 \\ 0 & \bar{\epsilon}_{22} - S_{2233}\bar{\sigma}_{33} & 0 \\ 0 & 0 & \bar{\epsilon}_{33} - S_{3333}\bar{\sigma}_{33} \end{pmatrix}. \tag{9}$$

Using the above expression, we can obtain the values of $\bar{\boldsymbol{\omega}}$ as a function of uniaxial external stress at different levels of damage or dose. Such homogenized information can be applied to continuum models directly due to the different length scales being considered.

We note that the total defect relaxation volume equals the total defect formation volume, as the total number of atoms is conserved. Therefore, the magnitude of volumetric swelling is readily obtained from the trace of $\bar{\boldsymbol{\omega}}$.

D. Crystal growth

We may understand crystal growth under irradiation through the change of simulation cell vectors [27]. One can write the matrix of cell vectors as:

$$\mathbf{L} = (\mathbf{L}_x, \mathbf{L}_y, \mathbf{L}_z) = \begin{pmatrix} L_{xx} & L_{yx} & L_{zx} \\ L_{xy} & L_{yy} & L_{zy} \\ L_{xz} & L_{yz} & L_{zz} \end{pmatrix}. \tag{10}$$

In the case of perfect lattice, this can be separated into two parts:

$$\mathbf{L} = \mathbf{PN}, \tag{11}$$

where $\mathbf{P}$ is the primitive cell vector matrix, and $\mathbf{N}$ represents the repetition of the primitive cell.

For the bcc lattice, the primitive cell vector matrix is

$$\mathbf{P} = \frac{a}{2} \begin{pmatrix} -1 & 1 & 1 \\ 1 & -1 & 1 \\ 1 & 1 & -1 \end{pmatrix}. \tag{12}$$

By inverting $\mathbf{P}$, one can get

$$\mathbf{N} = \begin{pmatrix} n_{xy} + n_{xz} & n_{yy} + n_{yz} & n_{zy} + n_{zz} \\ n_{xx} + n_{xz} & n_{yx} + n_{yz} & n_{zx} + n_{zz} \\ n_{xx} + n_{xy} & n_{yx} + n_{yy} & n_{zx} + n_{zy} \end{pmatrix}, \tag{13}$$

where $n_{ij} = L_{ij}/a$ represents the repetition of primitive cells in Cartesian coordinates.

In an orthogonal cell, we can write

$$\mathbf{N} = \begin{pmatrix} 0 & n_{yy} & n_{zz} \\ n_{xx} & 0 & n_{zz} \\ n_{xx} & n_{yy} & 0 \end{pmatrix}, \tag{14}$$

where n_{xx}, n_{yy}, n_{zz} is the number of unit cells in the x, y, and z directions, respectively.

In the case of a purely elastically deformed simulation cell, the primitive cell vector matrix can be written approximately according to linear elasticity as:

$$\mathbf{P}' = (\mathbf{I} + \boldsymbol{\epsilon}^e)\,\mathbf{P}, \tag{15}$$

where $\boldsymbol{\epsilon}^e = \mathbf{S}\boldsymbol{\sigma}$. On the other hand, we can also obtain the elastically deformed primitive cell from numerical calculations, which include non-linear contributions, where

$$\mathbf{P}' = \frac{1}{2} \begin{pmatrix} a_x & 0 & 0 \\ 0 & a_y & 0 \\ 0 & 0 & a_z \end{pmatrix} \cdot \begin{pmatrix} -1 & 1 & 1 \\ 1 & -1 & 1 \\ 1 & 1 & -1 \end{pmatrix}, \tag{16}$$

and a_x, a_y and a_z are the mean lattice parameters of an elastically deformed orthogonal unit cell in Cartesian coordinates. The three lattice parameters can be obtained from the deformed perfect simulation cell. We used this in our calculations.

When a simulation cell is subjected to irradiation, the crystal structure evolves. Assuming one can still identify the dominant crystal structure, we can estimate the number of repeating cells or planes along x, y, or z direction from:

$$\mathbf{N}' = \mathbf{P}'^{-1}\mathbf{L}', \tag{17}$$

where $\mathbf{L}'$ is the matrix of deformed cell vectors. The change of $\mathbf{N}'$ over the course of irradiation is attributed to the plastic deformation caused by the accumulation of defects.

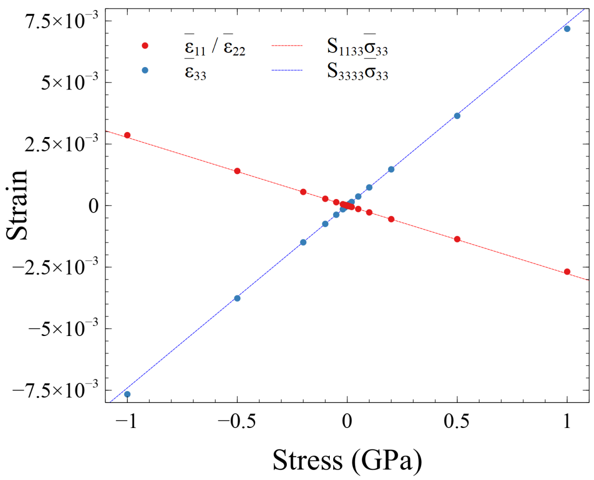

FIG. 1. The average strains of simulation cells subjecting to external uniaxial stresses. Linear elastic approximations are also plotted for comparison.

III. RESULTS

A. Change of macroscopic quantities

We will first examine the change of the average strain $\bar{\boldsymbol{\epsilon}}$ and the average relaxation volume density tensor $\bar{\boldsymbol{\omega}}$ as a function of irradiation dose in unit of DPA at various values of uniaxial stress. The $\bar{\boldsymbol{\epsilon}}$ at different conditions can be calculated from the simulation cell vectors, with reference to the perfect crystal lattice at 0 DPA and stress-free conditions.

Fig. 1 shows the $\bar{\boldsymbol{\epsilon}}$ of simulation cells subjected to different stress values at 0 DPA. We also plotted the corresponding linear elastic approximations. We observe that at stresses even as high as ±1 GPa linear elasticity offers an accurate description of the elastic strain. This validates the use of Eq. 9 to estimate the $\bar{\boldsymbol{\omega}}$.

The change of $\bar{\boldsymbol{\epsilon}}$ due to the application of external stress as a function of DPA is shown in Fig. 2. For visual clarity, we only plotted curves corresponding to large stress values. Although the starting values of $\bar{\boldsymbol{\epsilon}}$ are different, all components of $\bar{\boldsymbol{\epsilon}}$ increase linearly up to about 0.01 DPA, and non-linearly to about 0.03 DPA.

Similarly, we can observe the change of $\bar{\boldsymbol{\omega}}$ in Fig. 3. All components increase linearly up to about 0.01 DPA, and non-linearly to about 0.03 DPA, regardless of the applied stress. We note that now all values start from zero, meaning there are initially no defects in the system. The linear increment at low dose is due to the generation of isolated self-interstitial atoms (SIA) and vacancies [28]. We will further verify this point in following sections.

Beyond about 0.01 DPA, the values of $\bar{\boldsymbol{\epsilon}}$ and $\bar{\boldsymbol{\omega}}$ become stress dependent. For compressive stress in the z direction, the $\bar{\epsilon}_{11}$, $\bar{\epsilon}_{22}$, $\bar{\omega}_{11}$, and $\bar{\omega}_{22}$ increase, whereas $\bar{\epsilon}_{33}$ and $\bar{\omega}_{33}$ decrease. For tensile stress, the behavior is the other way around. According to previous CRA work [27–32],

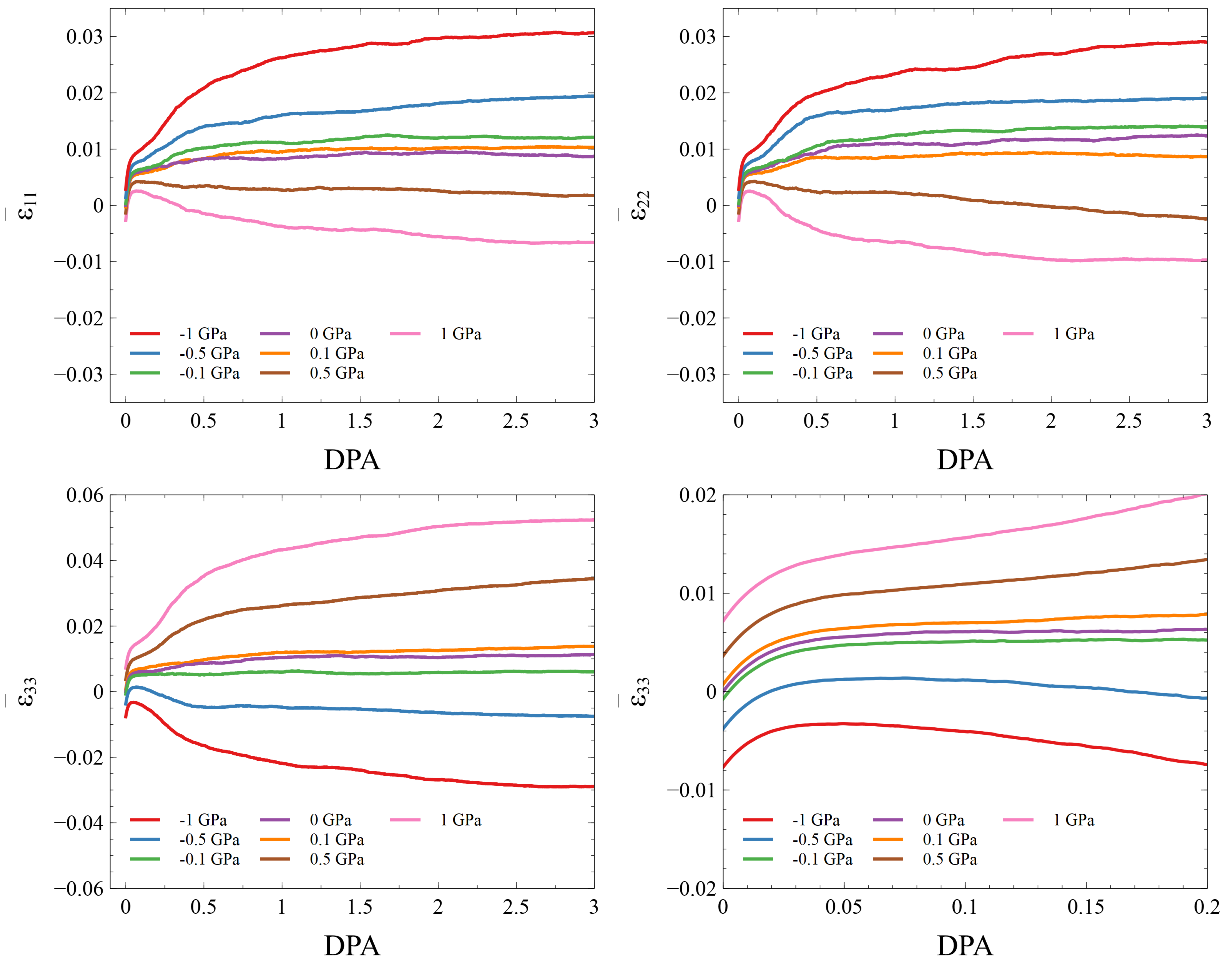

FIG. 2. The change of average strains as a function of dose in units of DPA.

beyond about 0.02 DPA, SIAs start clustering, forming dislocation loops, which is eventually followed by lattice plane formation.

Since the elastic field of a defect does not need to be isotropic, external stress $\sigma_{ij}^{\mathrm{ext}}$ can affect the energy of a system containing a defect, where the elastic energy of a defect subjecting to external field [43] can be written as $E_{\mathrm{el}} = -\sigma_{ij}^{\mathrm{ext}}\Omega_{ij}$, where Ω_{ij} is the defect relaxation volume tensor. It means the preferred orientation of defect clusters is biased by the external stress, which affects the orientations of subsequently formed lattice planes. By inspecting the change of $\bar{\boldsymbol{\omega}}$, we expect lattice planes to form preferentially with respect to the direction and value of stress. Mason *et al.* [31] show that in the case of a thin film, if the x and y dimension are constrained, lattice planes will form perpendicular to the z direction, which is similar to the tensile stress condition. We suggest a similar phenomenon is happening here, where further investigation will follow.

In Fig. 4, we plotted the $\bar{\boldsymbol{\epsilon}}$ against external uniaxial stress. We can observe the $\bar{\epsilon}_{11}$ and $\bar{\epsilon}_{22}$ decrease and $\bar{\epsilon}_{33}$ increase almost linearly with respect to stress. After eliminating the linear elastic effect, one can observe similar behavior of $\bar{\boldsymbol{\omega}}$ in Fig. 5. The main difference is that all the slopes are less steep. At 0 DPA, it is correctly observed that all $\bar{\boldsymbol{\omega}} = 0$.

At low dose below 0.2 DPA, components of $\bar{\boldsymbol{\omega}}$ show an almost linear relation to the external stress. However, when dose is larger than 0.2, and when the uniaxial stress is small, within ±0.1 GPa, we can observe fluctuation of data. There are two possible reasons. First, the fluctuation means simulation cells deform without preferential direction. Second, we cannot observe the bias properly due to insufficient simulations. Both reasons imply the external stress is not strong enough to affect the change of microstructure of current simulations.

We note that the dislocation density peaks at 0.2 DPA, at which point the microstructure contains larger dislocation loop due to the coalescence of smaller loops, at which point the dislocation network starts forming (we will discuss the microstructure below). The formation of dislocation networks reduces the ability of the system to respond to the external stress, since the energy barrier of changing the morphology of a dislocation network is

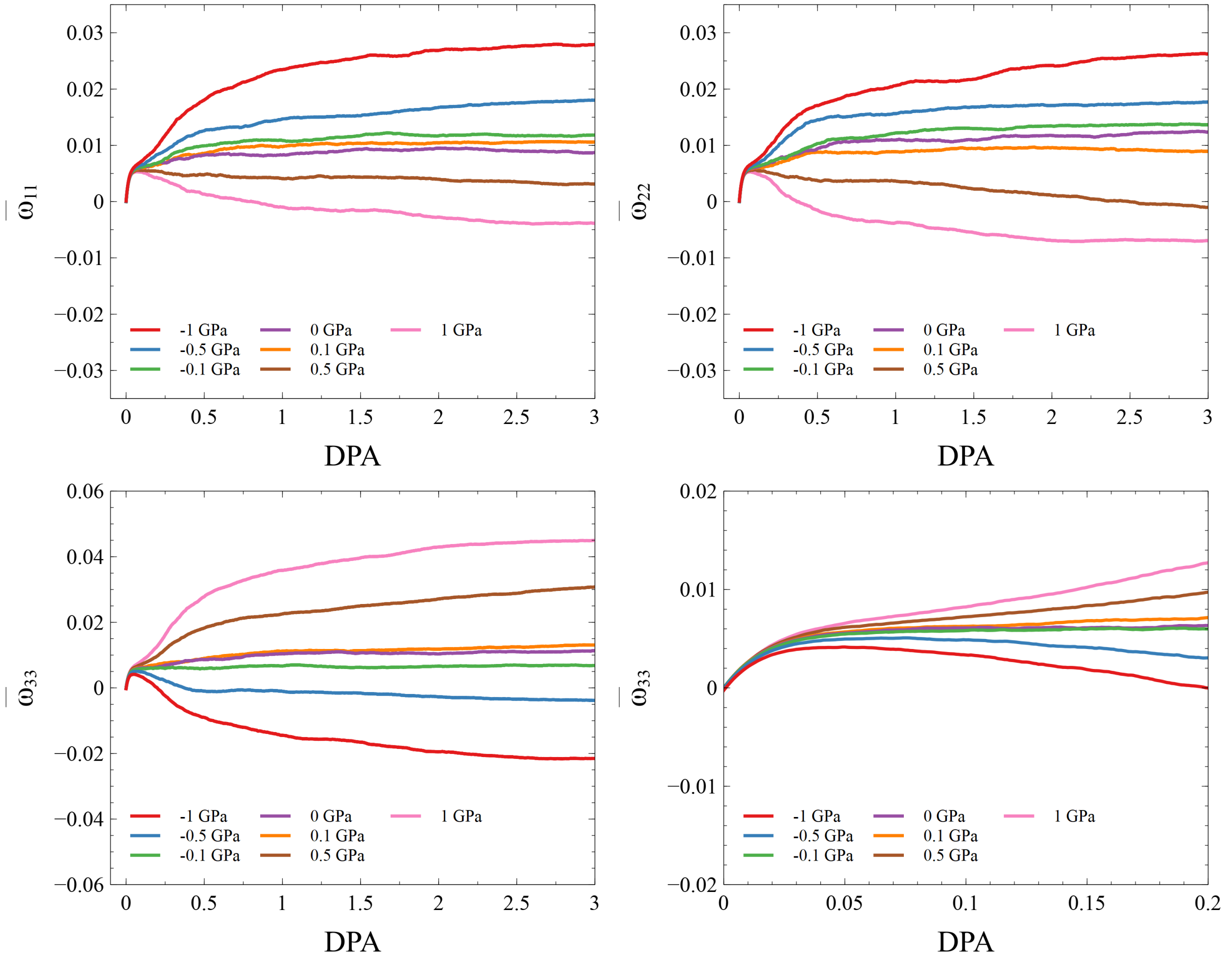

FIG. 3. The change of average relaxation volume density tensor as a function of dose in units of DPA.

much higher than for individual small loops and other localized defects.

We can inspect the spatial fluctuation of stress through the von Mises stress (VMS). VMS is often used in engineering to predict if a material will yield or fracture. The VMS σ_{vms} is relating to the Cauchy stress tensor σ_{ij} by

$$\begin{aligned}\sigma_{vms}^2 &= \frac{1}{2}[(\sigma_{11}-\sigma_{22})^2+(\sigma_{22}-\sigma_{33})^2+(\sigma_{33}-\sigma_{11})^2 \\ &\quad +6(\sigma_{23}^2+\sigma_{31}^2+\sigma_{12}^2)]\end{aligned} \tag{18}$$

The atomic VMS is defined according to the atomic Virial stress, which allows us to examine the spatial distribution of VMS.

Fig. 6 shows the spatially average and standard deviation of VMS. We can see there is little difference between large compressive and tensile stress, and stress-free conditions. On the other hand, we can see that at dose larger than 0.2 DPA, the $\bar{\boldsymbol{\omega}}$ show clear preferential behavior only when the absolute value of external stress is larger than 0.5 GPa, at which point its magnitude is comparable to the VMS. One possible explanation is that in order to affect the microstructural evolution of a dislocation network as it is forming, external stress needs to be able to induce an energy change comparable to the energy scale of the network as a whole, rather than to the energy scale of individual defects. Consequently, the response of the system changes for dose larger than 0.2 DPA.

We try to map $\bar{\boldsymbol{\omega}}$ to simple functions. This may help developing other continuum models, such as FEM. We assume $\bar{\omega}_{11}$ and $\bar{\omega}_{22}$ are degenerate, i.e. $\bar{\omega}_{11}=\bar{\omega}_{22}$. We found that we can fit $\bar{\omega}_{11}$ and $\bar{\omega}_{33}$ to simple functions of dose and external stress. We write:

$$\begin{aligned}\bar{\omega}_{11}(\phi,\bar{\sigma}_{33}) &= m_1(\phi)\,\bar{\sigma}_{33}+c_1(\phi)\\ \bar{\omega}_{33}(\phi,\bar{\sigma}_{33}) &= m_3(\phi)\,\bar{\sigma}_{33}+c_3(\phi),\end{aligned} \tag{19}$$

where ϕ is the dose. After performing least-squares fitting to all data, we get

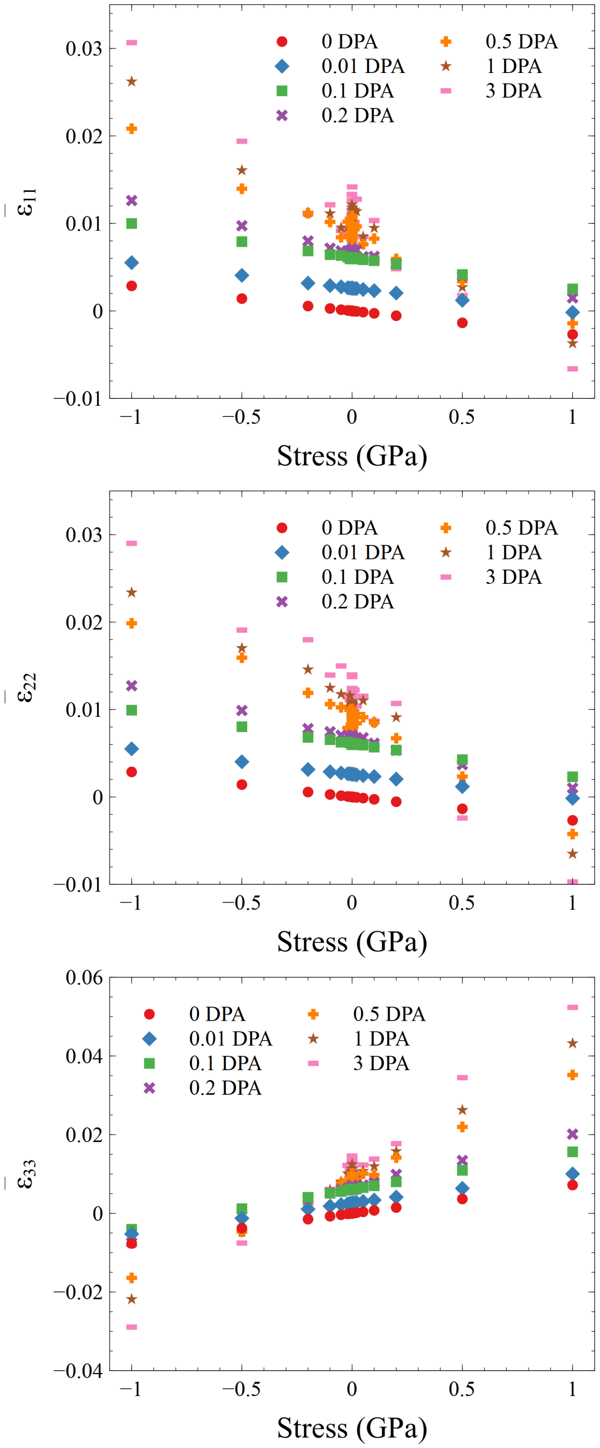

FIG. 4. The average strain as a function of stress at different doses in units of DPA.

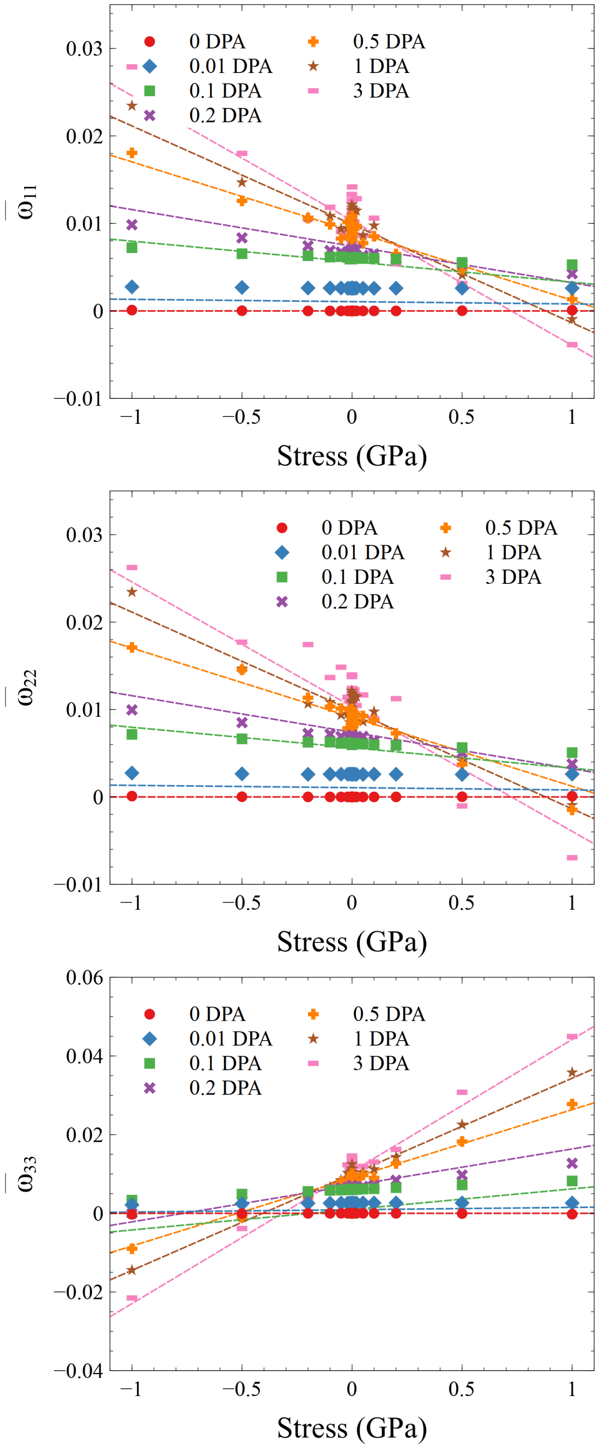

FIG. 5. The average relaxation volume density tensor as a function of stress at different doses in units of DPA. Dotted lines are plotted according to fitting functions (Eq. 19).

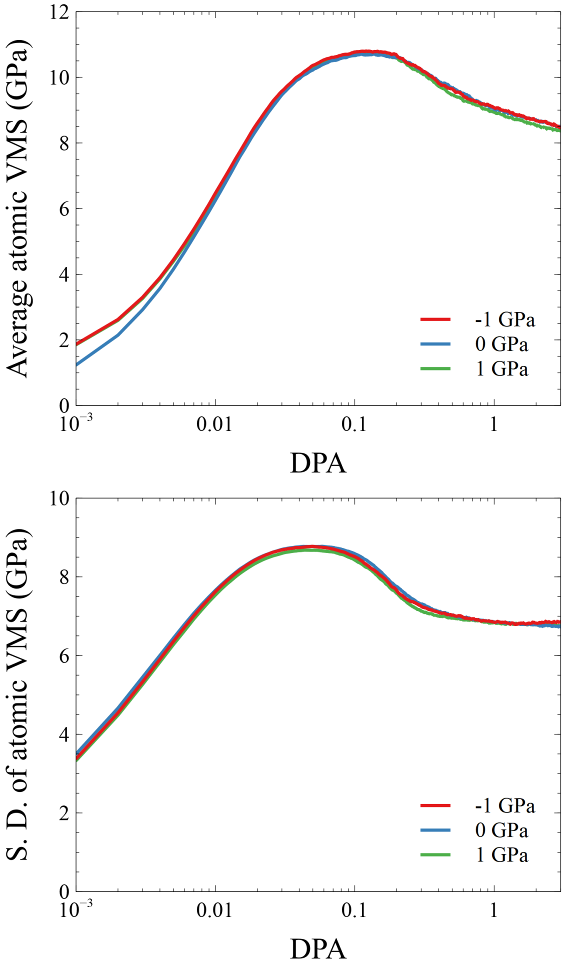

FIG. 6. Spatially average and the standard deviation of the von Mises stress (VMS) as a function of dose in units of DPA.

$$
\begin{aligned}
m_1(\phi) &= \frac{-\phi}{37.57527287 + 51.30537329\phi}\mathrm{GPa}^{-1} \\
c_1(\phi) &= \frac{\phi}{8.50780179 + 92.60261486\phi} \\
m_3(\phi) &= \frac{\phi}{16.73788571 + 24.20713517\phi}\mathrm{GPa}^{-1} \\
c_3(\phi) &= \frac{\phi}{10.03662945 + 90.76207731\phi}.
\end{aligned}
\tag{20}
$$

In Fig. 7, we show the corresponding three dimensional plot of the two fitted functions. Error is shown as a heat-map projected on the floor.

B. Irradiation-induced swelling and creep

In general, swelling is represented by the change of volumetric strain

$$
\epsilon_v = \frac{V - V_0}{V_0}, \tag{21}
$$

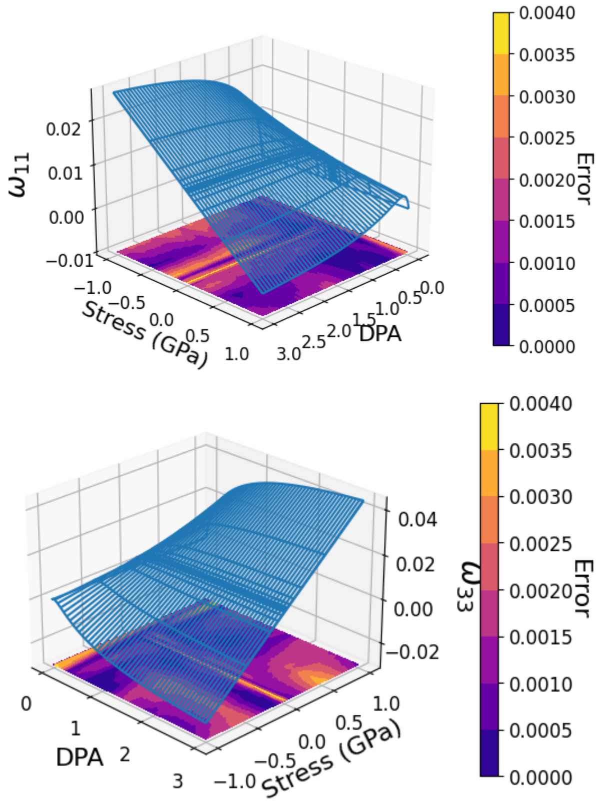

FIG. 7. The 11 (or 22) and 33 components of the relaxation volume density tensor fitted as a function of stress and dose. The error is visualized as a heat-map on the floor.

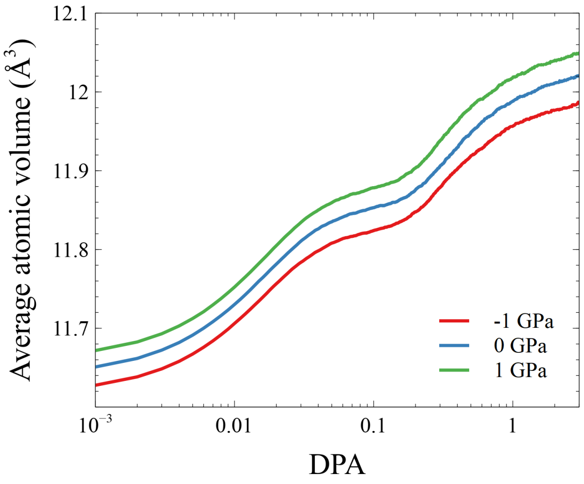

FIG. 8. The average atomic volume as a function of dose.

where V and V_0 are current and initial volume. The initial volume V_0 is the volume of external stress deformed cell at 0 DPA, not the stress-free cell. We plotted the change of the average atomic volume and the volumetric strain as a function of dose in Fig. 8 and 9, respectively. The swelling rate at different stresses is about 3% at high

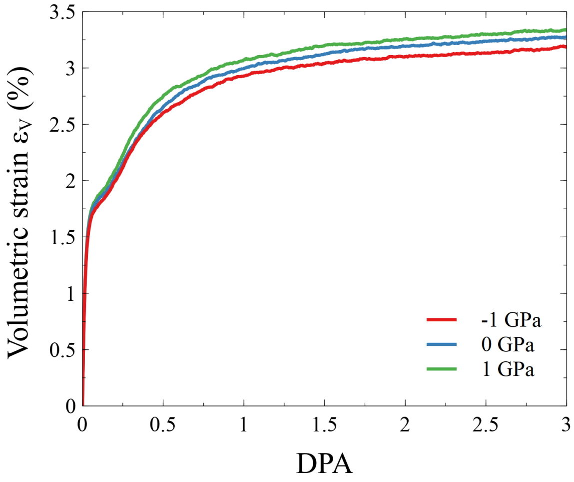

FIG. 9. The volumetric strain as a function of dose. The swelling at 3 DPA is about 3%.

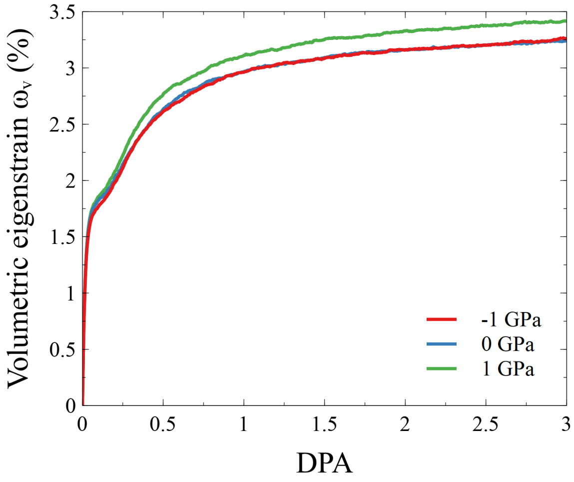

FIG. 10. The volumetric eigenstrain as a function of dose.

dose, which is compatible with previous works by Derlet and Dudarev using other interatomic potentials [28].

We can see the atomic volume are not the same at different stress values, even before irradiation. We may understand that even in isotropic materials, the elastic deformation of the volume due to uniaxial external applied stresses is in general not zero, because

$$\epsilon_v^e = Tr(\boldsymbol{\epsilon}^e) = \epsilon_{11}^e + \epsilon_{22}^e + \epsilon_{33}^e = \frac{1-2\nu}{E}\sigma_{app}, \qquad (22)$$

where E is the Young modulus and ν is the Poisson's ration. We can observe that for $\nu < 0.5$, when σ_{app} is positive, the volumetric elastic strain represented by ϵ_v^e should be positive. It is compatible with what we can see in Fig. 8.

In fact, within linear (anisotropic) elasticity, we can

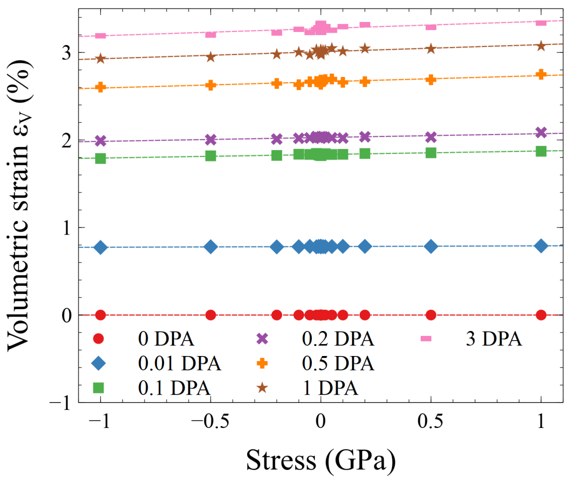

FIG. 11. The volumetric strain as a function of stress at different dose.

rewrite Eq. 21 into

$$\epsilon_v = \frac{(1+Tr(\boldsymbol{\epsilon}))V^p - (1+Tr(\boldsymbol{\epsilon}^e))V^p}{(1+Tr(\boldsymbol{\epsilon}^e))V_p} \qquad (23)$$

where V^p is the volume of stress-free unirradiated perfect lattice cell. One can simplify it into

$$\epsilon_v = \frac{\omega_v}{1+Tr(\boldsymbol{\epsilon}^e)} \approx \omega_v \qquad (24)$$

where $\omega_v = \bar{\omega}_{11} + \bar{\omega}_{22} + \bar{\omega}_{33}$, which is the volumetric eigenstrain. One can approximate $\epsilon_v \approx \omega_v$, because ϵ_v, ϵ_v^e and ω_v are in the same order. In linear elasticity, terms higher than the first order are ignored.

The volumetric eigenstrain corresponds to the plastic deformation only. It is plotted in Fig. 10. The plastic strain is also at about 3% at high dose. We can see the volumetric strain and eigenstrain are very close to each other as expected.

Both ϵ_v and ω_v are mildly stress dependent. We inspect the stress dependent of them in Fig. 11 and 12. We can see a seemingly linear relation where the swelling increases as tensile stress increases. Linear fittings were performed to find the slopes. We should note ω_{ij} is calculated assuming linear elasticity according to Eq. 9. The values of ω_{ij} at ±1 GPa may not be very accurate by observing Fig. 1. In Fig. 13, it shows the slopes of linear fittings of Fig. 11 and 12 and other similar data. We can see the slopes saturate at about 8×10^{-4} GPa^{-1}. The effect of stress on volumetric swelling exists, but is small.

Regarding irradiation-induced creep, it may be separated into two parts from experimental perspective. They are creep in the absence of swelling and swelling enhanced creep [22, 24]. In the linear regime, it has been described by a phenomenological equation:

$$\epsilon^p/\sigma_{app} = B_0\phi + D\epsilon_v \qquad (25)$$

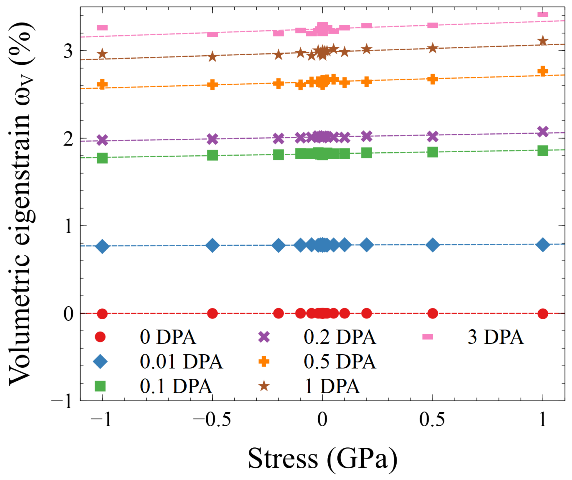

FIG. 12. The volumetric eigenstrain as a function of stress at different dose.

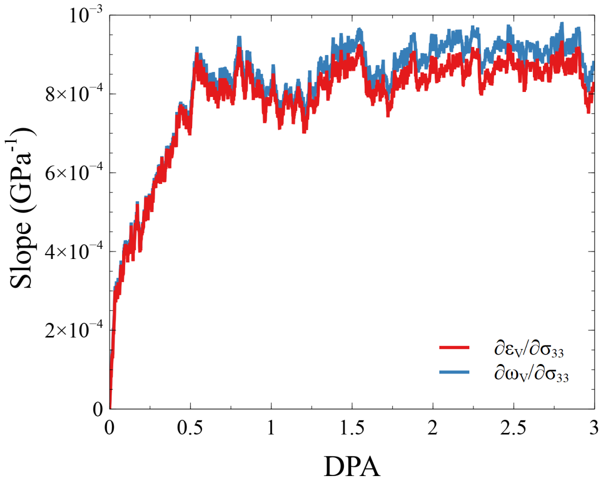

FIG. 13. The slope of linear fit to the volumetric strain or eigenstrain versus stress as a function of dose.

where ϵ^p is the plastic strain, σ_{app} is the applied stress, B_0 is the creep compliance for irradiation creep deformation, and D is the creep-swelling coupling coefficient for irradiation creep deformation. This equation applies to cases where the plastic strain increases as the dose increases, and swelling is comparatively small.

In our simulations, the plastic strain $\epsilon^p = \bar{\omega}_{33}$ and $\sigma_{app} = \sigma_{33}$. We can separate the eigenstrain $\bar{\boldsymbol{\omega}}$ into two parts according to above logic, namely the hydrostatic volumetric swelling ω_v and volume conserved creep $\boldsymbol{\omega}'$, such that

$$\omega'_{ij} = \bar{\omega}_{ij} - \frac{\delta_{ij}}{3}\omega_v. \tag{26}$$

Using the approximation $\epsilon_v \approx \omega_v$, we can rewrite Eq. 25 into

$$\frac{\omega'_{33}}{\sigma_{app}} + \frac{\omega_v}{3\sigma_{app}} = B_0\phi + D\omega_v. \tag{27}$$

We can see the first and second terms on both sides have the same physical meaning, respectively. It suggests the coefficient $D = 1/(3\sigma_{app})$, which is not really a coefficient.

For the coefficient B_0, we need to inspect ω'_{ij}, which is shown in Fig. 14. The ω'_{33} is monotonic increasing or decreasing according to the sign of external stress. The ω'_{11} and ω'_{22} have opposition sign to ω'_{33}. The external stress is clearly responsible for creep. However, they are not linearly increasing or decreasing. They saturate at high dose limit. Only at low dose below 0.2 DPA, we can observe near linear behaviour.

We plotted in Fig. 15, the value of ω'_{33}/σ_{33} against the dose ϕ below 0.2 DPA. The slopes of them are essentially the coefficient B_0, which is about 0.3 GPa^{-1} DPA^{-1}. It is much larger than 0.5×10^{-3} GPa^{-1} DPA^{-1} in ferritic steels [49]. We should note experiment is usually performed at 0.2 to 0.45 of T_m (melting temperature) [22], which is much higher than the vacancy migration temperature. Therefore, more defects are annihilated in the process. In our simulations using CRA, they are in the athermal regime. The diffusion of defects were inhabited. Besides, our simulations are on pure iron. Alloying and impurity effects are omitted. However, current results remain a plausible way to examine the underlying mechanism of swelling and creep due to irradiation.

C. Microstructure evolution

We examined the change of microstructure subjected to various external uniaxial stresses. We used OVITO [50] to perform analysis and visualization of samples.

First, we analyze the content of point defects. Point defects were identified by Wigner-Seitz analysis, which is implemented in OVITO. In each Voronoi volume of the reference lattice site, one can count the number of atoms corresponding to the displaced configuration. The reference configuration is the initial defect-free simulation cell at 0 DPA. A Voronoi volume having no atom is considered as vacancy, while a volume with two atoms occupancy is considered as an SIA. Voronoi volumes with three atoms occupancy or higher are rare, so we can safely discard them.

Similar to the work by Derlet and Dudarev [28], we further identify the isolated and non-isolated SIAs, but we used a different criteria. We classify an SIA as belonging to a cluster if there is another SIA within a specified cutoff distance. We used a cutoff of 3.2 Å, which is a distance between the second and third nearest neighbors of an atom in the perfect iron bcc lattice. Since Wigner-Seitz analysis places SIAs on reference lattice sites, which here are lattice points of the perfect crystal, our results remain the same for any cutoff distance between a and $\sqrt{2}a$, or 2.9 Å and 4.0 Å, respectively.

In the work of Derlet and Dudarev [28], they identified the isolated SIAs if there is no other atom sitting within a cutoff of 0.93 of $\sqrt{3}a/2$, which is approximately 2.3 Å

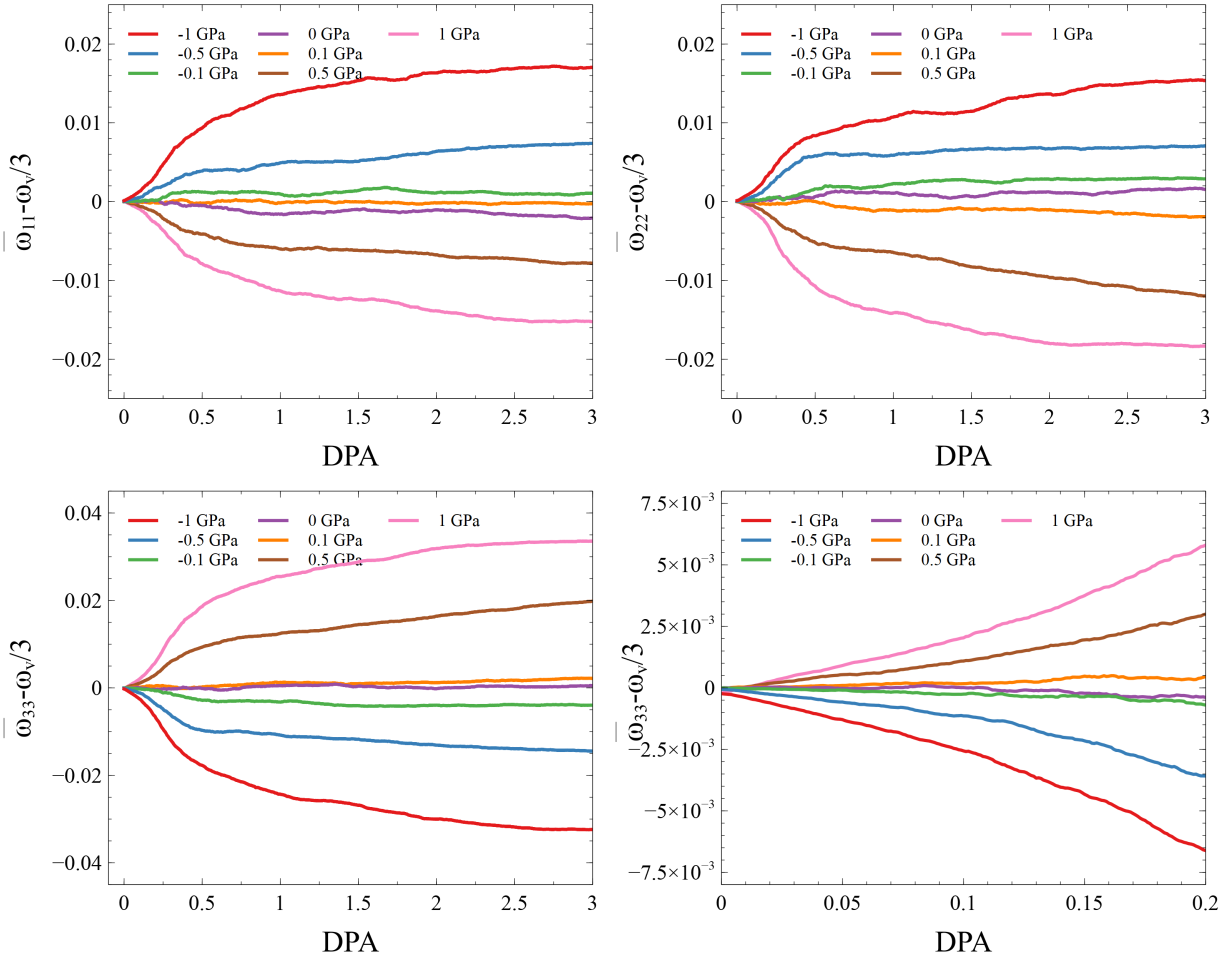

FIG. 14. The change of average strains minus 1/3 of the volumetric strain as a function of dose in units of DPA.

for bcc iron. However, we should remember that 2 atoms sit within a Voronoi volume of a reference lattice site, it only has 1 SIA. It is ambiguous to tell which one is the SIA, and so the atomic position. If both are considered as SIA, it is double counting the total number of SIA. Instead, if we only consider the reference lattice site, we know the exact location of an SIA.

In Fig. 16, it shows the vacancy and isolated SIA contents. Interestingly, we can see there is little difference between samples at ±1 GPa and stress-free conditions. All of them reach a maximum isolated SIA concentration at around 0.03 DPA. The vacancy and isolated SIA concentrations start diverging at around 0.01 DPA, where larger defect clusters such as dislocation loops and SIA clusters are forming. At high dose, the vacancy and isolated interstitial contents reach a steady state with concentrations of 4.2% and 0.8%, respectively. They are in quantitative agreement with work by Derlet and Dudarev [28] using two other interatomic potentials.

Then, we analyzed the Laves phases cluster size. We identified the Laves phases using the polyhedral template matching (PTM) method [51]. According to Chartier and Marinica [33], one could identify the C15 Laves phases by finding the icosahedral structure. Essentially, C14, C15 and C36 Laves phases are made of Z12 and Z16 Frank-Kasper clusters. Z12 means icosahedral arrangement with 12 neighboring atoms. Z16 is a similar arrangement but with 16 neighboring atoms. PTM can only identify icosahedral arrangements, but since C15 is expected to stabilized in irradiated iron, they argued that the identification of Z12 is equivalent to C15, where independent analysis [52] confirmed this. We note that another method to identify different Laves phases was developed by Xie *et al.* [53].

Cluster analysis is used for the analysis of the sizes of Laves phases clusters. Cluster analysis uses a cutoff distance similar to the coordination analysis. For any given particle, they are iteratively added to particular cluster. Finally, we got the cluster sizes and know which particle belong to which cluster.

In Fig. 17, we plot the cluster size against the dose in units of DPA. Counting of clusters is shown as color map. One can observe a bright spot at around 0.1 DPA, corresponding to the peak quantity. Our results are in qual-

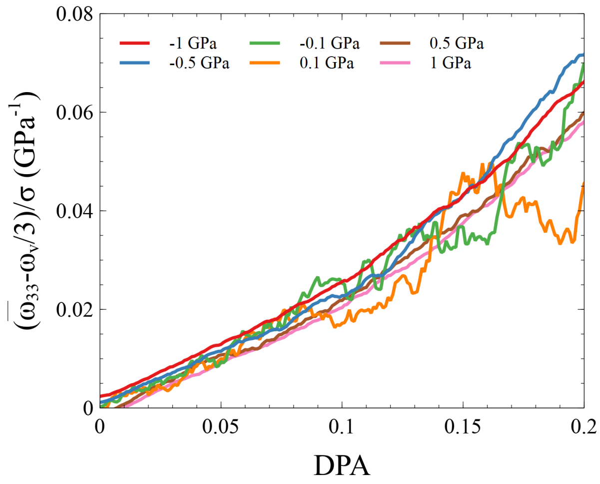

FIG. 15. The change of strains minus 1/3 of the volumetric strain divided by the apply stress as a function of dose in units of DPA.

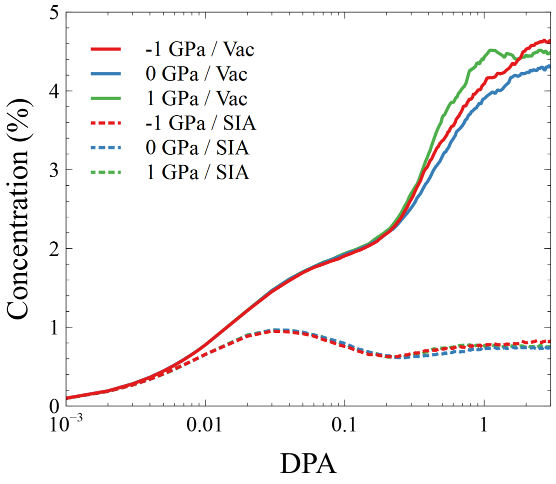

FIG. 16. Vacancy and isolated self-interstitial at 1, 0 and -1 GPa

itative agreement with work by Chartier and Marinica [33]. We obtained a larger number of Laves phase clusters, where the sizes of clusters are smaller than results by Chartier and Marinica. A possible reason is that they are using a different interatomic potential and working at finite temperature. Fig. 18 shows the volume concentration of clusters as a function of dose. Similarly, we see a peak in cluster concentration at around 0.1 DPA, after which the concentrations drop and eventually reach steady values. It is because some of the clusters are transforming into dislocation loops [33]. Interestingly, we found external stress to have little effect on the cluster content.

Finally, we analyzed the dislocation density. Dislocation analysis (DXA) [54] being implemented in OVITO is used to identify the length and nature of dislocations. Figure 19 shows the dislocation density for different Burgers vectors. The dislocation content peaks at around 0.2 to 0.25 DPA, after which it drops gradually. Only dislocations of $\frac{a}{2}\langle 111\rangle$ and $a\langle 100\rangle$ type are observed, which $\frac{a}{2}\langle 111\rangle$-type dislocations having significantly higher content. These observations agree with similar simulations [28, 33]. The relative formation energy of $\frac{a}{2}\langle 111\rangle$ and $a\langle 100\rangle$ dislocations and C15 clusters [55] explains the relative densities as well as the point at which Laves phases cluster concentration starts to

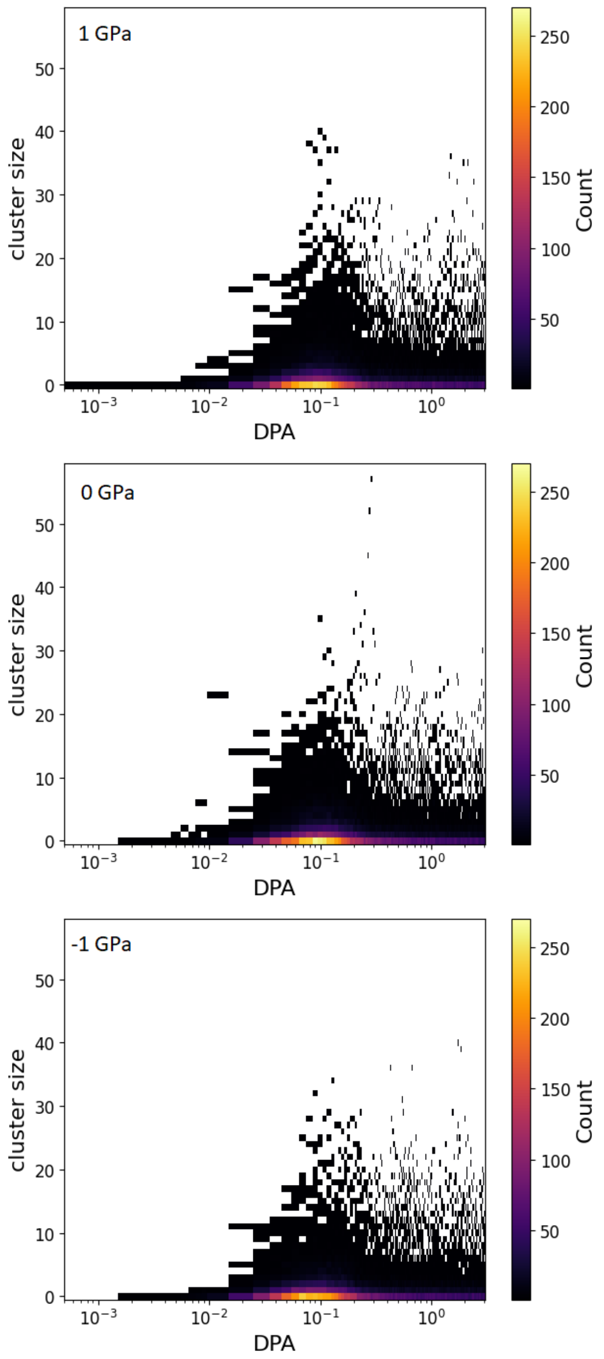

FIG. 17. Laves phase cluster size distribution as a function of dose at (top) 1, (middle) 0, and (bottom) -1 GPa.

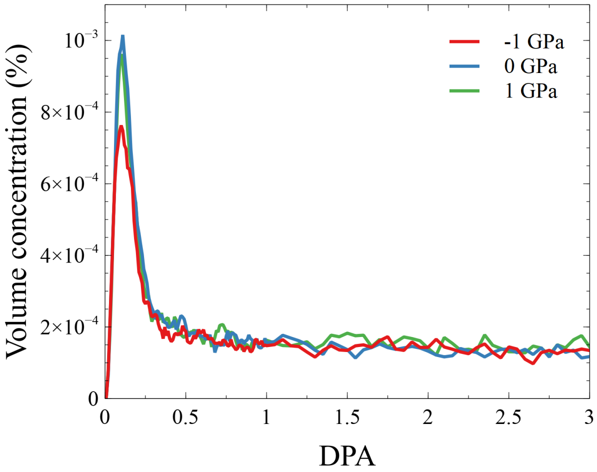

FIG. 18. Volume concentration of Laves phase clusters at -10,000, 0, and 10,000 bars.

drop while dislocation density starts to rise, where Laves phases clusters nucleate dislocation loops [33, 55].

Again, we do not see any evidence that external uniaxial stresses in the range of ±1 GPa affects the dislocation density and type in comparison to stress-free conditions.

In Fig. 20, we show the microstructural content of isolated SIAs, vacancies, dislocations and Laves phases clusters side-by-side. It gives us a better idea of the spatial distribution of defects. Since we found they behave similarly at different external stress, we only plotted the stress-free samples. We can observe clearly that the content of isolated SIAs drops and vacancies increases starting from 0.01 DPA. On the other hand, the Laves phases cluster is peak at 0.1 DPA, where dislocation is peak at 0.2 DPA. It is corroborate with the explanation that Laves phases clusters are transforming into dislocation loops [33].

According to what we found here, it appears that the microstructure in relation to isolated SIAs, vacancies, Laves phases clusters, and dislocations is not affected by the external uniaxial stress. These defects are not the main cause of the change and polarization of the $\bar{\omega}$ under external uniaxial stresses.

D. Anisotropic planes formation

The anisotropy of $\bar{\omega}$ is indicative of the polarization of defects formed during irradiation. As we found the content of isolated defects to be unaffected by application of external uniaxial stress, we expect the anisotropy of $\bar{\omega}$ to be caused by anisotropic crystal growth. The $\bar{\omega}$ of different stresses start diverging at around 0.2 DPA, at which point dislocations start coalescing, forming dislocation networks and eventually lattice planes [28]. Experimentally [24], the number and size of dislocation loops in AISI 316 stainless steel under stress have been studied.

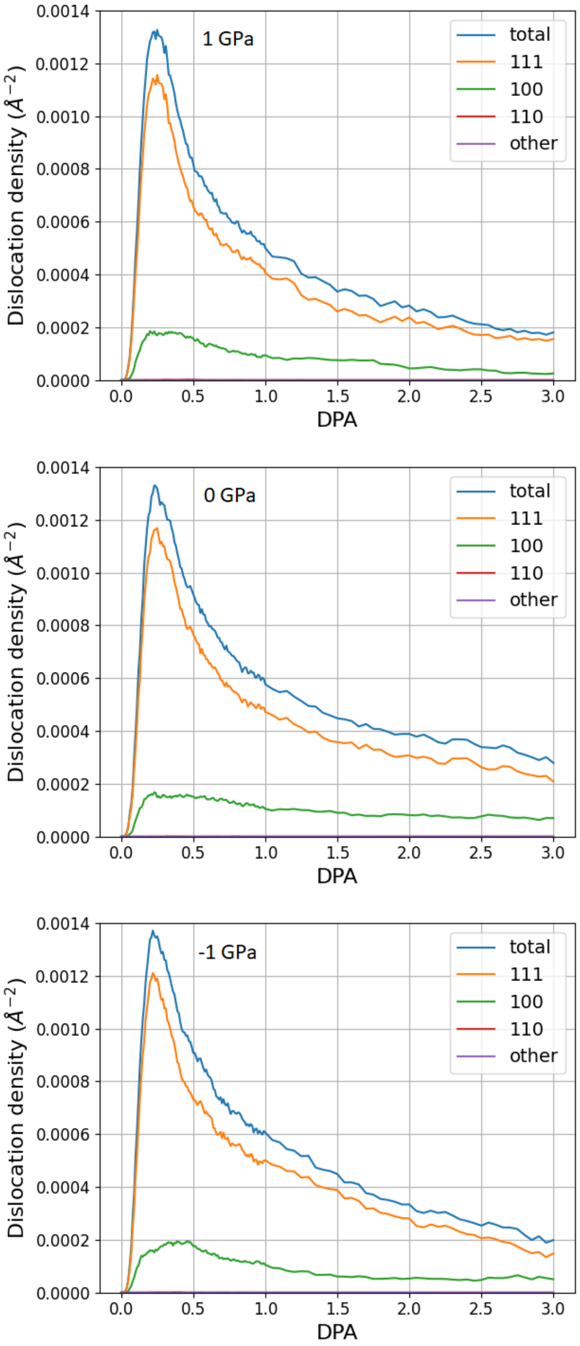

FIG. 19. Dislocation density for different burgers vectors at (top) 1, (middle) 0, and (bottom) -1 GPa.

The loop number density increases in the lattice planes normal to the applied stress, with a decrease in number of loop orientations parallel to stress, but the loop size distributions are not changed by an applied stress. We argue that the external applied stress leads to a preferential orientation of plane growth, leading to the anisotropic changes in $\bar{\omega}$.

To test this hypothesis, we identify and visualize non-isolated SIAs, see Fig. 21. We can clearly observe that

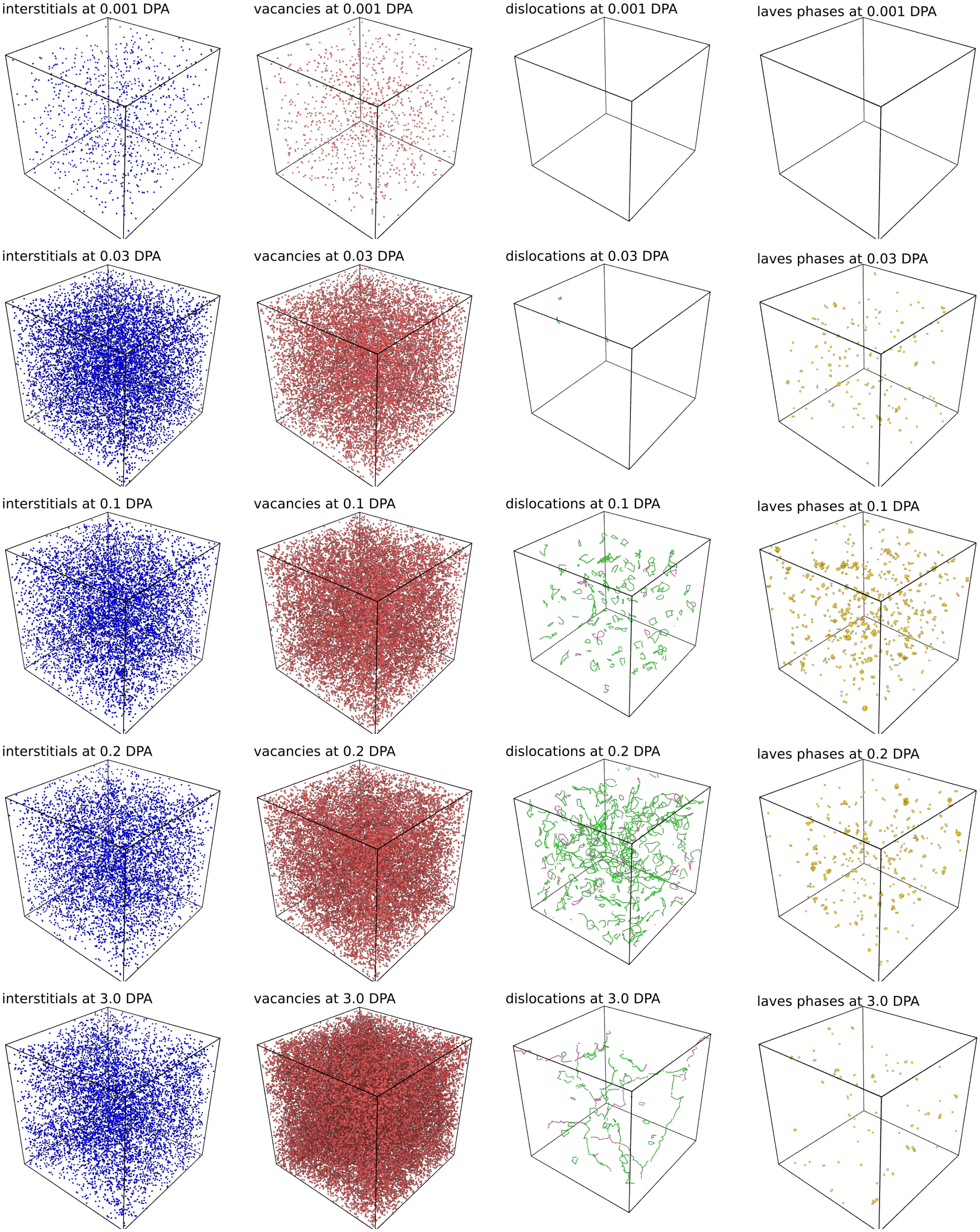

FIG. 20. Isolated self-interstitials, vacancies, dislocations, and Laves phases clusters at different irradiation dose.

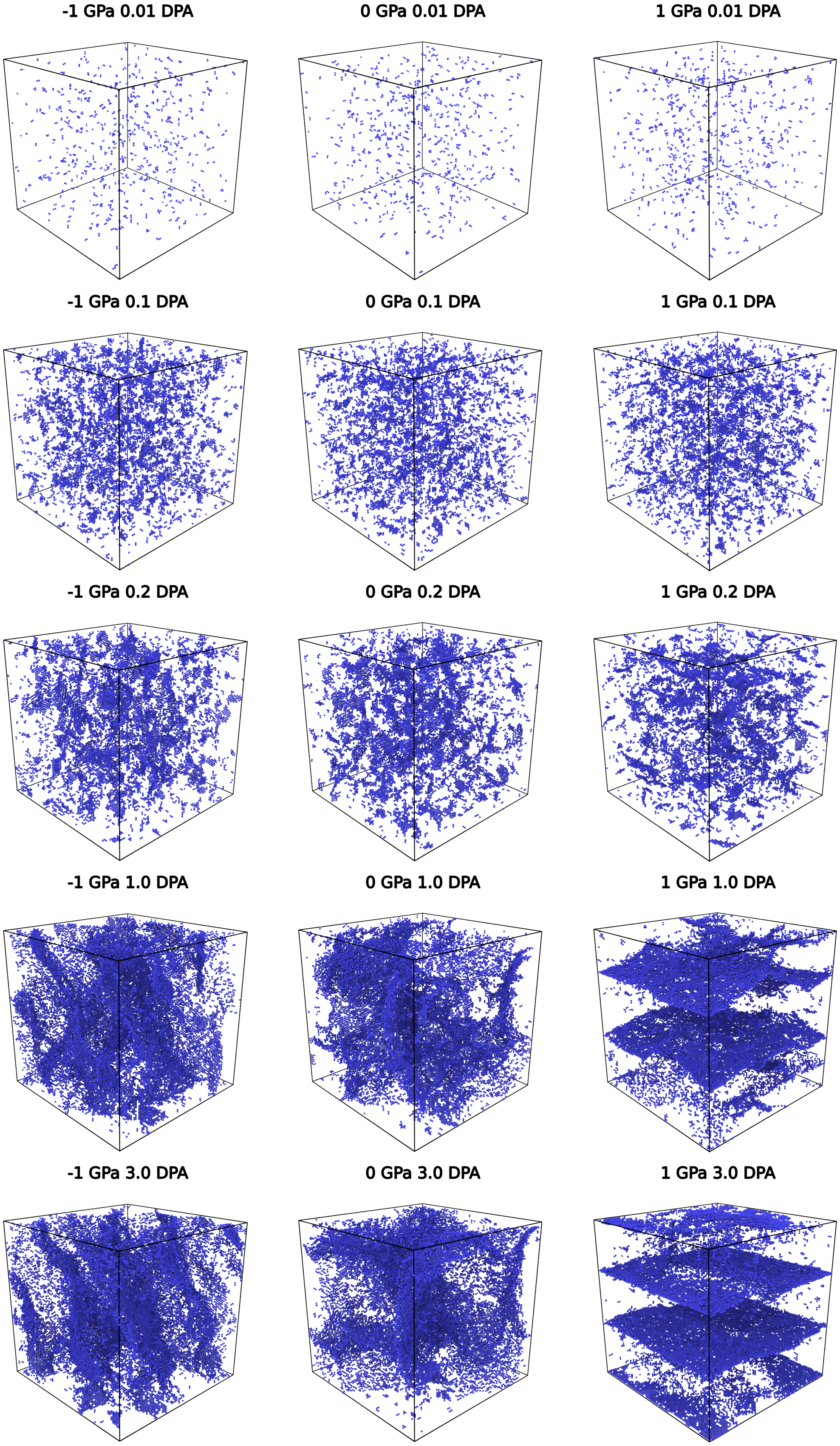

FIG. 21. Non-isolated self-interstitial defects forming clusters and extra planes of atoms.

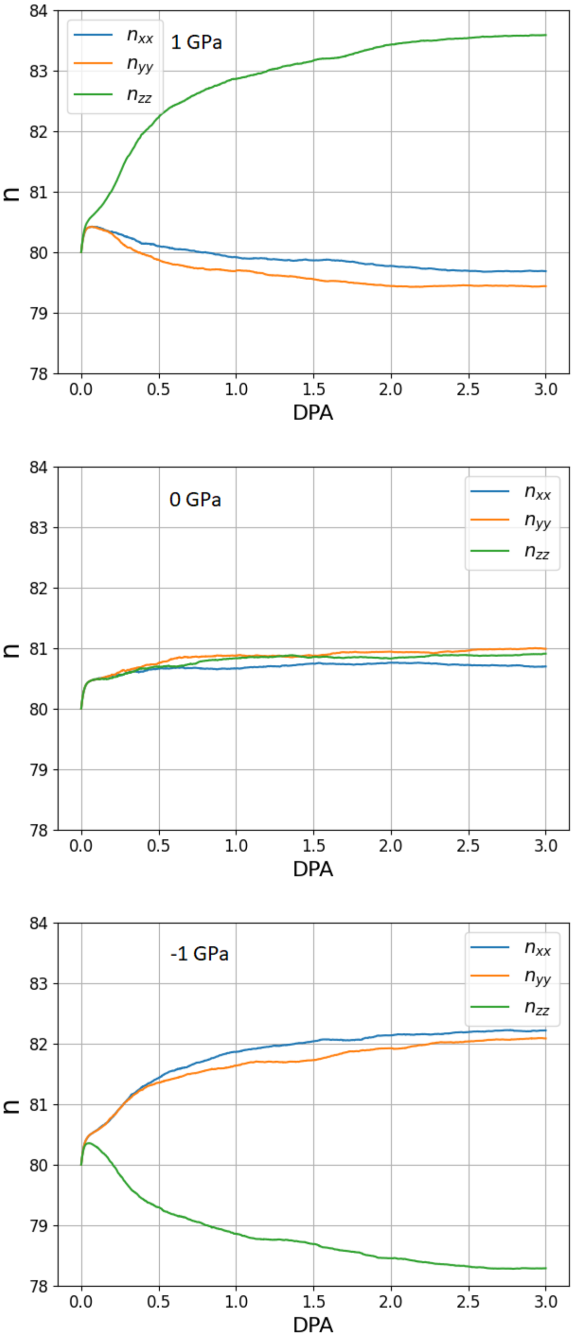

FIG. 22. Total number of repeating unit cells as a function dose at (top) 1, (middle) 0, and (bottom) -1 GPa.

when a system is subjected to tensile stress, planes are forming perpendicular to the uniaxial loading direction. This finding is corroborated by the CRA simulations by Mason *et al.* [31, 32], where it was found that interstitial planes form normal to the z direction when cell dimensions are constrained in x and y directions to mimic a scenario where the sample is attached to a fixed substrate. When our samples are subjected to compressive stress, the orientation of plane growth is less obvious.

We may quantify the changes by assuming the relation between cell vectors and repetition of unit cells. In Fig. 22, we can observe the change of n_{xx}, n_{yy} and n_{zz}. When a system is under tensile stress of 1 GPa, the n_{zz} increases from 80 to slightly higher than 83. We can compare this with Fig. 21, where we can see about 3 planes are formed. In the case of compressive stress, we can see n_{xx} and n_{yy} reach 82, while n_{zz} drops to 78.5. We can understand planes are forming such that they contribute to growth in the x and y direction, but diminishing in the z direction.

We may conclude from this data that the anisotropy of $\bar{\omega}$ under external stress is caused by the stress-dependent orientation of the formed interstitial planes.

IV. CONCLUSION

We performed simulations of heavily irradiated iron under uniaxial stress using the creation-relaxation algorithm. Irradiation-induced swelling and creep are discussed through the change of the defect relaxation volume density (or eigenstrain). We can observe eigenstrain of defects showing anisotropic changes when stress is applied. Such polarization starts occurring at around 0.1 to 0.2 DPA, where self-interstitial forms dislocation loops, followed by the formation of dislocation networks.

We investigated the microstructure. We found the application of external stress to have little effect on the density of isolated SIAs, vacancies, Laves phases clusters, and dislocations, and vice versa. On the other hand, the anisotropic changes of $\bar{\omega}$ are due to the anisotropic growth of interstitial planes driven by the external stress. Tensile stress leads to a preferential formation of planes with normals collinear to the loading direction, while compressive stress leads to a more complex pattern of planes with normals perpendicular to the loading direction.

We should note that our results obtained by CRA are essentially simulating conditions where thermal diffusion of defects is suppressed, for instance because the temperature is low or by the presence of impurities. They may be comparable with experiment through rescaling [28, 30], but the scaling relations are not straightforward. Quantities obtained from CRA simulations and experiments can differ by a factor of 10 [31]. We note that collision cascade simulations with low recoil energies ($\sim$ 100 eV) can reach defect contents comparable to CRA [56], hence part of the mismatch can be attributed to the lack of defect recombination arising from higher-energy recoils present in realistic irradiation conditions. However, we can still see quantitative agreement between simulations and experiments [38], which allows us to infer the principal mechanisms underlying certain phenomena at a fraction of the cost of conventional cascade simulations.

ACKNOWLEDGMENTS

We acknowledge stimulating discussion with Daniel R. Mason. Luca Stefanescu contributed to this work as a part of an internship at the United Kingdom Atomic Energy Authority, Culham Science Centre, Abingdon, Oxfordshire, OX14 3DB, United Kingdom. This work has been carried out within the framework of the EUROfusion Consortium, funded by the European Union via the Euratom Research and Training Programme (Grant Agreement No 101052200 — EUROfusion) and from the EPSRC [grant number EP/W006839/1]. To obtain further information on the data and models underlying this paper please contact PublicationsManager@ukaea.uk. Views and opinions expressed are however those of the author(s) only and do not necessarily reflect those of the European Union or the European Commission. Neither the European Union nor the European Commission can be held responsible for them. The authors acknowledge the use of the Cambridge Service for Data Driven Discovery (CSD3) and associated support services provided by the University of Cambridge Research Computing Services (www.csd3.cam.ac.uk) in the completion of this work.

[1] H. Tanigawa, E. Gaganidze, T. Hirose, M. Ando, S. Zinkle, R. Lindau, and E. Diegele, Development of benchmark reduced activation ferritic/martensitic steels for fusion energy applications, Nuclear Fusion **57**, 092004 (2017).

[2] D. Stork, P. Agostini, J.-L. Boutard, D. Buckthorpe, E. Diegele, S. L. Dudarev, C. English, G. Federici, M. R. Gilbert, S. Gonzalez, A. Ibarra, C. Linsmeier, A. L. Puma, G. Marbach, L. W. Packer, B. Raj, M. Rieth, M. Q. Tran, D. J. Ward, and S. J. Zinkle, Materials R&D for a timely DEMO: Key findings and recommendations of the EU Roadmap Materials Assessment Group, Fusion Engineering and Design **89**, 1586–1594 (2014).

[3] F. A. Garner, M. B. Toloczko, and B. H. Sencer, Comparison of swelling and irradiation creep behavior of fcc-austenitic and bcc-ferritic/martensitic alloys at high neutron exposure, Journal of Nuclear Materials **276**, 123–142 (2000).

[4] D. S. Gelles, Void swelling in pFeCr alloys at 200 dpa, Journal of Nuclear Materials **225**, 163–174 (1995).

[5] M. Norgett, M. Robinson, and I. Torrens, A proposed method of calculating displacement dose rates, Nuclear Engineering and Design **33**, 50 (1975).

[6] A. E. Sand, S. L. Dudarev, and K. Nordlund, High-energy collision cascades in tungsten: Dislocation loops structure and clustering scaling laws, EPL (Europhysics Letters) **103**, 46003 (2013).

[7] A. E. Sand, K. Nordlund, and S. L. Dudarev, Radiation damage production in massive cascades initiated by fusion neutrons in tungsten, Journal of Nuclear Materials **455**, 207 (2014), Proceedings of the 16th International Conference on Fusion Reactor Materials (ICFRM-16).

[8] A. E. Sand, M. J. Aliaga, M. J. Caturla, and K. Nordlund, Surface effects and statistical laws of defects in primary radiation damage: Tungsten vs. iron, EPL (Europhysics Letters) **115**, 36001 (2016).

[9] A. E. Sand, D. R. Mason, A. D. Backer, X. Yi, S. L. Dudarev, and K. Nordlund, Cascade fragmentation: deviation from power law in primary radiation damage, Materials Research Letters **5**, 357 (2017).

[10] D. R. Mason, A. E. Sand, X. Yi, and S. L. Dudarev, Direct observation of the spatial distribution of primary cascade damage in tungsten, Acta Materialia **144**, 905 (2018).

[11] X. Yi, A. E. Sand, D. R. Mason, M. A. Kirk, S. G. Roberts, K. Nordlund, and S. L. Dudarev, Direct observation of size scaling and elastic interaction between nano-scale defects in collision cascades, EPL (Europhysics Letters) **110**, 36001 (2015).

[12] R. Alexander, M.-C. Marinica, L. Proville, F. Willaime, K. Arakawa, M. R. Gilbert, and S. L. Dudarev, Ab initio scaling laws for the formation energy of nanosized interstitial defect clusters in iron, tungsten, and vanadium, Phys. Rev. B **94**, 024103 (2016).

[13] F. Hofmann, D. R. Mason, J. K. Eliason, A. A. Maznev, K. A. Nelson, and S. L. Dudarev, Non-contact measurement of thermal diffusivity in ion-implanted nuclear materials, Scientific Reports **5** (2015).

[14] S. Cui, R. P. Doerner, M. J. Simmonds, C. Xu, Y. Wang, E. Dechaumphai, E. Fu, G. R. Tynan, and R. Chen, Thermal conductivity degradation and recovery in ion beam damaged tungsten at different temperature, Journal of Nuclear Materials **511**, 141 (2018), Special Section on 18th International Conference on Fusion Reactor Materials.

[15] A. Reza, H. Yu, K. Mizohata, and F. Hofmann, Thermal diffusivity degradation and point defect density in self-ion implanted tungsten, Acta Materialia **193**, 270 (2020).

[16] A. Hasegawa, M. Fukuda, S. Nogami, and K. Yabuuchi, Neutron irradiation effects on tungsten materials, Fusion Engineering and Design **89**, 1568 (2014), Proceedings of the 11th International Symposium on Fusion Nuclear Technology-11 (ISFNT-11) Barcelona, Spain, 15-20 September, 2013.

[17] M. Durrand-Charre, *Microstructure of Steels and Cast Irons* (Springer-Verlag, Berlin, 2003).

[18] E. Gaganidze, C. Petersen, E. Materna-Morris, C. Dethloff, O. J. Weiß, J. Aktaa, A. Povstyanko, A. Fedoseev, O. Makarov, and V. Prokhorov, Mechanical properties and TEM examination of RAFM steels irradiated up to 70 dpa in BOR-60, Journal of Nuclear Materials **417**, 93–98 (2011).

[19] C. Cabet, F. Dalle, E. Gaganidze, J. Henry, and H. Tanigawa, Ferritic-martensitic steels for fission and fusion applications, Journal of Nuclear Materials **523**, 510–537 (2019).

[20] K. Ochiai, S. Sato, H. Kondo, M. Ohta, M. Oyaidzu, M. Nakamura, S. Kwon, H. Tanigawa, T. Nozawa, A. Kasugai, K. Sakamoto, and S. Ishida, Conceptual design progress of advanced fusion neutron source, Nuclear Fu-

sion **61**, 025001 (2020).
[21] M. R. Gilbert, S. Zheng, R. Kemp, L. W. Packer, S. L. Dudarev, and J.-C. Sublet, Comparative assessment of material performance in demo fusion reactors, Fusion Science and Technology **66**, 9 (2014).
[22] S. J. Zinkle, H. Tanigawa, and B. D. Wirth, Chapter 5 - radiation and thermomechanical degradation effects in reactor structural alloys, in *Structural Alloys for Nuclear Energy Applications*, edited by G. R. Odette and S. J. Zinkle (Elsevier, Boston, 2019) pp. 163–210.
[23] J. Matthews and M. Finnis, Irradiation creep models — an overview, Journal of Nuclear Materials **159**, 257 (1988).
[24] K. Ehrlich, Irradiation creep and interrelation with swelling in austenitic stainless steels, Journal of Nuclear Materials **100**, 149 (1981).
[25] F. Granberg, J. Byggmästar, and K. Nordlund, Molecular dynamics simulations of high-dose damage production and defect evolution in tungsten, Journal of Nuclear Materials **556**, 153158 (2021).
[26] C. A. Hirst, F. Granberg, B. Kombaiah, P. Cao, S. Middlemas, R. S. Kemp, J. Li, K. Nordlund, and M. P. Short, Revealing hidden defects through stored energy measurements of radiation damage, Science Advances **8**, eabn2733 (2022).
[27] M. Boleininger, S. L. Dudarev, D. R. Mason, and E. Martínez, Volume of a dislocation network, Physical Review Materials **6**, 10.1103/physrevmaterials.6.063601 (2022).
[28] P. M. Derlet and S. L. Dudarev, Microscopic structure of a heavily irradiated material, Phys. Rev. Materials **4**, 023605 (2020).
[29] J. Tian, H. Wang, Q. Feng, J. Zheng, X. Liu, and W. Zhou, Heavy radiation damage in alpha zirconium at cryogenic temperature: A computational study, Journal of Nuclear Materials **555**, 153159 (2021).
[30] A. R. Warwick, M. Boleininger, and S. L. Dudarev, Microstructural complexity and dimensional changes in heavily irradiated zirconium, Physical Review Materials **5**, 113604 (2021).
[31] D. R. Mason, S. Das, P. M. Derlet, S. L. Dudarev, A. J. London, H. Yu, N. W. Phillips, D. Yang, K. Mizohata, R. Xu, and F. Hofmann, Observation of transient and asymptotic driven structural states of tungsten exposed to radiation, Phys. Rev. Lett. **125**, 225503 (2020).
[32] D. R. Mason, F. Granberg, M. Boleininger, T. Schwarz-Selinger, K. Nordlund, and S. L. Dudarev, Parameter-free quantitative simulation of high-dose microstructure and hydrogen retention in ion-irradiated tungsten, Phys. Rev. Materials **5**, 095403 (2021).
[33] A. Chartier and M. C. Marinica, Rearrangement of interstitial defects in alpha-Fe under extreme condition, Acta Materialia **180**, 141–148 (2019).
[34] L. Reali, M. Boleininger, M. R. Gilbert, and S. L. Dudarev, Macroscopic elastic stress and strain produced by irradiation, Nuclear Fusion **62**, 016002 (2021).
[35] G. J. Ackland, M. I. Mendelev, D. J. Srolovitz, S. Han, and A. V. Barashev, Development of an interatomic potential for phosphorus impurities in α-iron, Journal of Physics: Condensed Matter **16**, S2629 (2004).
[36] M. P. Allen and D. J. Tildesley, *Computer Simulation of Liquids*, Oxford science publications (Clarendon Press, 1987).
[37] S. Plimpton, Fast parallel algorithms for short-range molecular dynamics, Journal of Computational Physics **117**, 1 (1995).
[38] S. Wang, W. Guo, T. Schwarz-Selinger, Y. Yuan, L. Ge, L. Cheng, X. Zhang, X. Cao, E. Fu, and G.-H. Lu, Dynamic equilibrium of displacement damage defects in heavy-ion irradiated tungsten, Acta Materialia , 118578 (2022).
[39] T. Mura, *Micromechanics of defects in solids* (Kluwer Academic Publishers, 1998).
[40] P.-W. Ma and S. L. Dudarev, Universality of point defect structure in body-centered cubic metals, Phys. Rev. Materials **3**, 013605 (2019).
[41] P.-W. Ma and S. L. Dudarev, Calanie: Anisotropic elastic correction to the total energy, to mitigate the effect of periodic boundary conditions, Computer Physics Communications , 107130 (2019).
[42] P.-W. Ma and S. L. Dudarev, Symmetry-broken self-interstitial defects in chromium, molybdenum, and tungsten, Phys. Rev. Materials **3**, 043606 (2019).
[43] P.-W. Ma and S. L. Dudarev, Effect of stress on vacancy formation and migration in body-centered-cubic metals, Phys. Rev. Materials **3**, 063601 (2019).
[44] P.-W. Ma and S. L. Dudarev, Nonuniversal structure of point defects in face-centered cubic metals, Phys. Rev. Materials **5**, 013601 (2021).
[45] D. R. Mason, D. Nguyen-Manh, M.-C. Marinica, R. Alexander, A. E. Sand, and S. L. Dudarev, Relaxation volumes of microscopic and mesoscopic irradiation-induced defects in tungsten, Journal of Applied Physics **126**, 075112 (2019).
[46] P.-W. Ma, D. R. Mason, and S. L. Dudarev, Multiscale analysis of dislocation loops and voids in tungsten, Phys. Rev. Materials **4**, 103609 (2020).
[47] S. L. Dudarev, D. R. Mason, E. Tarleton, P.-W. Ma, and A. E. Sand, A multi-scale model for stresses, strains and swelling of reactor components under irradiation, Nuclear Fusion **58**, 126002 (2018).
[48] A. P. Sutton, *Physics of Elasticity and Crystal Defects* (Oxford University Press, Oxford, England, 2020) p. 39.
[49] F. A. Garner, M. B. Toloczko, and B. H. Sencer, Comparison of swelling and irradiation creep behavior of fcc-austenitic and bcc-ferritic/martensitic alloys at high neutron exposure, Journal of Nuclear Materials **276**, 123 (2000).
[50] A. Stukowski, Visualization and analysis of atomistic simulation data with OVITO - the open visualization tool, Modelling and Simulation in Materials Science and Engineering **18**, 10.1088/0965-0393/18/1/015012 (2010).
[51] P. M. Larsen, S. Schmidt, and J. Schiøtz, Robust structural identification via polyhedral template matching, Modelling and Simulation in Materials Science and Engineering **24**, 055007 (2016).
[52] A. M. Goryaeva, C. Lapointe, C. Dai, J. Dérès, J.-B. Maillet, and M.-C. Marinica, Reinforcing materials modelling by encoding the structures of defects in crystalline solids into distortion scores, Nature Communications **11**, 4691 (2020).
[53] Z. Xie, D. Chauraud, E. Bitzek, S. Korte-Kerzel, and J. Guénolé, Laves phase crystal analysis (LaCA): Atomistic identification of lattice defects in C14 and C15 topologically close-packed phases, Journal of Materials Research **36**, 2010 (2021).
[54] A. Stukowski, V. V. Bulatov, and A. Arsenlis, Automated identification and indexing of dislocations in crystal in-

terfaces, Modelling and Simulation in Materials Science and Engineering **20**, 085007 (2012).

[55] J. Byggmästar and F. Granberg, Dynamical stability of radiation-induced c15 clusters in iron, Journal of Nuclear Materials **528**, 151893 (2020).

[56] M. Boleininger, D. R. Mason, A. E. Sand, and S. L. Dudarev, Microstructure of a heavily irradiated metal exposed to a spectrum of atomic recoils, arXiv preprint arXiv:2210.05010 https://doi.org/10.48550/arXiv.2210.05010 (2022).